Engineering and Computational Mechanics
Volume 165 Issue EM2

Simulations of double-diffusive convection in narrow containers
Dimitrova, Pol, Webb and Fernando

ice | proceedings

Proceedings of the Institution of Civil Engineers
Engineering and Computational Mechanics 165 June 2012 Issue EM2
Pages 131–145 http://dx.doi.org/10.1680/eacm.10.00027
Paper 1000027
Received 20/05/2010 Accepted 28/10/2010
Keywords: dynamics/mathematical modelling/thermal effects

ice Institution of Civil Engineers publishing

Simulations of double-diffusive convection in narrow containers

Reneta Dimitrova
Research Assistant Professor, Environmental Fluid Dynamics Laboratories, Department of Civil Engineering and Geological Sciences, University of Notre Dame, Notre Dame, Indiana, USA

Suhas Pol
Post-Doctoral Research Associate, Los Alamos National Laboratory, Los Alamos, New Mexico, USA

Stephen Webb
Distinguished Member of Technical Staff, Geoscience and Environmental Center, Sandia National Laboratories, Albuquerque, New Mexico, USA

Harindra J. S. Fernando
Wayne and Diana Murdy Professor, Civil Engineering and Geological Sciences, University of Notre Dame, Notre Dame, Indiana, USA

A numerical investigation was conducted on the evolution of double-diffusive layers in a narrow-aspect-ratio cylinder that contains a salt-stratified fluid and subjected to bottom and side-wall heating. The numerical results were compared with the data of a laboratory experimental study conducted in parallel. The simulations were carried out using the Fluent computational fluid dynamics code, with a modified shear-stress k–ω transport model to better account for buoyancy effects. The role of the turbulence model in numerical predictions was investigated by conducting laminar and turbulent flow simulations. Both the experimental and numerical results show formation of multiple mixed layers of fluid separated by diffusive interfaces. Comparisons of laboratory and numerical results show a very good agreement for the layer thicknesses and not such good agreement for the temperature and salinity structures. The reasons for disparities between the model and experimental results were identified.

Notation

d	diameter of the cylinder
G_b	source term of turbulent kinetic energy
$\boldsymbol{g}$	gravitational constant
H	height
k	turbulent kinetic energy
N	buoyancy frequency
Pr_t	turbulent Prandtl number
p	pressure
S	salinity
T	temperature
W	width
z	vertical coordinate
α	thermal expansion coefficient
β	salinity contraction coefficient
Δb	initial buoyancy frequency
ΔT_0	initial temperature difference
δ	layer thickness
ε	turbulent dissipation rate
μ_t	turbulent viscosity
ρ	fluid density
ω	specific dissipation rate

1. Introduction

Double-diffusive convection occurs in a stably stratified fluid with two solutes of disparate molecular diffusivities when one of the solutes contributes a stable stratification and the other an unstable stratification. This phenomenon has been studied extensively; pertinent reviews can be found in Turner (1974, 1985) and Kelly *et al.* (2003). The most common example is the oceanic double diffusion, where the faster and slower diffusing substances are the heat and salt, respectively (Brandt and Fernando, 1996; Turner, 1967). Applications also abound in such areas as geophysics, astrophysics, metallurgy and chemistry (Huppert and Turner, 1981). Without loss of generality, in the following, the fast-diffusing substance is referred to as heat and the slow-diffusing substance as salt. A particularly interesting case of double diffusion arises when a stable salt gradient is heated from below (Fernando, 1987, 1988, 1989), where a layered structure forms and heat and mass transfer take place between the layers through (diffusive) interfaces. A variant of this case is the formation of a layered structure when a salinity stratified fluid is heated or cooled at vertical or inclined side walls (Chen *et al.*, 1971; Fedorovich and Shapiro, 2009; Huppert *et al.*, 1984; Hyun and Lee, 1989; Lee and Hyun, 1991; Lee *et al.*, 1988; Lin and Armfield, 1999; Nishimura *et al.*, 1999; Suzukawa and Narusawa, 1982; Thorpe *et al.*, 1969). This paper falls into this latter class of problems, wherein layered structure forms when a salinity stratified fluid is heated from both the sides and bottom. Both numerical simulations and laboratory experiments were conducted simultaneously, and the focus here is numerical modelling and model evaluation. To the present authors' knowledge studies on this particular problem have not been reported in the literature. A brief overview of the experiment is given in Section 2, followed by discussions on numerical modelling (Section 3), results (Section 4) and conclusions (Section 5).

The current interest in this problem is application to the US strategic petroleum reserves (SPR). Oil from various countries is stored in underground salt caverns. During the fill process, a stable stratification is set up by the mixing of (paraffin) oils (i.e. solvent) with different naphthene (solute) contents. Geothermal

heat flux from the sides and bottom of SPR caverns introduces heat as a diffusing component, and double-diffusive layers from the two solutes (heat and naphthalene) occur in the oil stored in the caverns. Issues of general interest are the formation, thicknesses and breakdown of these layers during storage – as well as during withdrawal and reinjection – which occur during periodic degasification of the oil. It is the former that is of interest in the present paper.

In order to understand the physical processes occurring in the caverns, numerical simulation of double-diffusive convection has been undertaken using a commercial computational fluid dynamics (CFD) code. This selection was driven by the need for a code amenable to complex geometries so that it can be implemented in actual SPR caverns (typically 2000 ft (609·6 m) high and 200 ft (69·96 m) in diameter). The numerical model has been evaluated using laboratory experiments, which were heated from the sides and bottom of a small-aspect-ratio (width/height) tank containing linearly stratified salt water. In all, the objectives were to

(*a*) develop a reliable numerical model, validated by laboratory studies, to be used in SPR operations
(*b*) clarify the mechanisms of multiple layer formation for this particular configuration including the impact of turbulence.

2. Experiment

The combined bottom/side-wall heating experiments were conducted using a transparent long glass cylinder filled with an initially linearly stratified fluid. The aspect ratio of the cylinder was $W/H = 1/8$, with a height $H = 80$ cm and width $W = 10$ cm. This cylinder was submersed in a temperature-controlled, gently stirred, hot water bath to provide the bottom and side-wall heating (Figure 1). Flow visualisation was conducted by dropping crystals of potassium permanganate close to the inner walls of the cylinder, which formed thin dye streaks as they descended to the bottom. Upon heating, the dye streaks distorted and followed the mean circulation while smearing off owing to turbulent diffusion. A micro-scale conductivity/salinity probe was used to record the microstructure. Sixteen experiments were conducted with the buoyancy frequency N in the range 0·29–1·24/s and the initial temperature difference ΔT_0 in the range 4·2–17·8°C (Pol, 2010). Given the focus on numerical aspects, only a single experiment is discussed here, but the results presented are quite general.

In the experiment described here, the inner cylinder was filled with salt stratified water at room temperature (25°C) with a buoyancy frequency of $N \sim 0{\cdot}44$/s. The well-known two-bucket system was employed to achieve the initial stratification in the experimental vessel (Oster and Yamamoto, 1963), which also allowed for the establishment of different buoyancy frequencies. The experimental cylinder was suspended within an external bath with a controlled temperature of 37°C, which provided the boundary condition for the inner cylinder. After some time, several mixed layers of almost identical vertical heights were formed, as shown in Figure 2, except that the bottom layer was thicker owing to enhanced mixing caused by both the side and bottom heating. The dark centre at the top of the bottom layer indicates a convergence zone, where part of the heated fluid at the side walls converges towards the centre and descends, forming convective cells.

Figure 1. Apparatus for the side and bottom heating of a salinity stratified fluid

The temperature and salinity profiles were taken at the centre of the cylinder at different times (2, 5 and 8 min) from the beginning of heating (Figure 3). Clearly, the topmost layers are of similar height and fluid in the individual layers is well mixed. The salt transport through the layers is much slower than that of heat, as seen from the salinity and temperature profiles, the former remaining essentially unchanged over the 8 min shown. A distinct jump in salinity can be observed between various mixed layers, causing a buoyancy difference that sustains a stable diffusive interface. Owing to higher heat diffusivity, nevertheless,

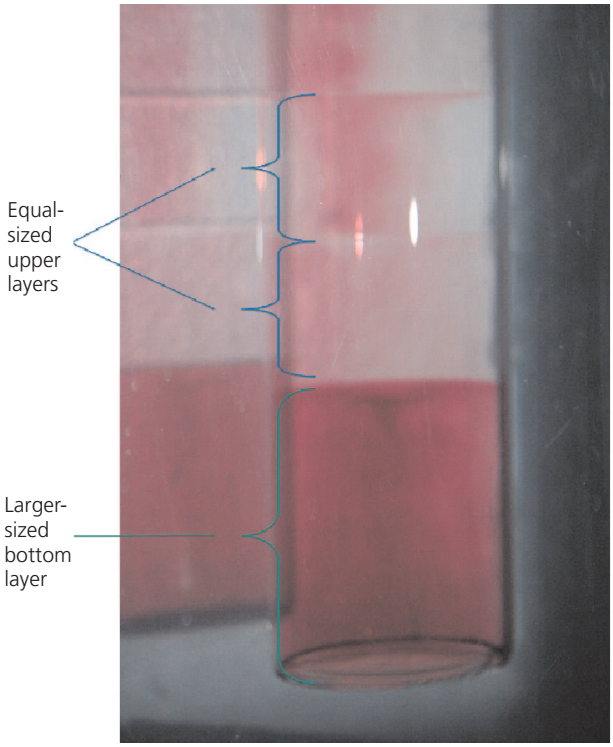

Figure 2. Multiple layers formation (the front image is the actual cylinder; the back image is a reflection off the back wall of the outer tank)

the temperature jump across various mixed layers changes rapidly. The bottom-most mixed layer is maintained at a higher temperature compared to those of upper layers, owing to heating from the bottom as well as the sides.

3. Numerical modelling

The Fluent version 6.2 (*Fluent 6.2 User's Guide* (Ansys, 2005)) CFD software was employed in this study. Fluent is a state-of-the-art commercial CFD code that solves the fundamental Navier–Stokes equations for mass, momentum and energy through a finite-volume approach including buoyancy and turbulence. The species transport (sodium chloride) module without reactions was used to solve for the double-diffusive mixing problem pertinent to the inner cylinder, and a second-order implicit transient solution was used to capture the layer evolution. The segregated solver was selected, as the governing equations are solved sequentially (i.e. segregated from one another). As the governing equations are coupled and non-linear, several iterations of the solution loop needed to be performed before a converged solution could be obtained. The PISO (pressure implicit with splitting of operators) method was used for pressure–velocity coupling, the Presto (pressure staggering option) method for pressure discretisation, and second-order upwind discretisation was used for momentum, turbulence, energy and species transport. The convergence during the simulations was judged by monitoring the residuals. The time step was considered converged when all normalised residuals were less than 10–3, except for energy and species transport equations for which the residuals

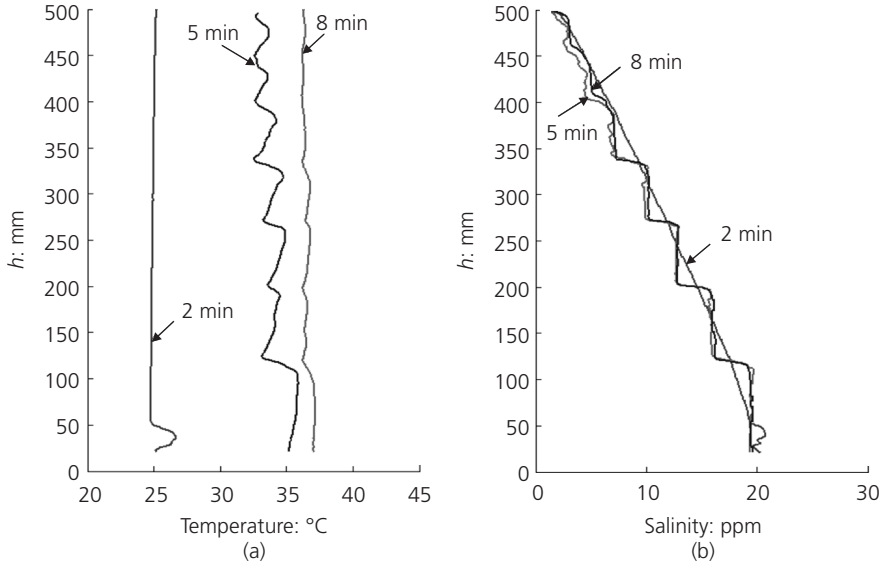

Figure 3. Profiles of temperature and salinity at the centre of the cylinder at different times – 2, 5 and 8 min from the beginning of heating (initial conditions: wall temperature 37°C; bottom salinity 23 g/l)

were less than 10−6. The typical time step for simulations was ~ 0·01 s. A value of 0 was specified as the operating density. The operating pressure was specified as 101 325 Pa (1 atm) on the top of the cylinder. Wall boundary conditions were applied to the sides and the bottom of the cylinder (constant temperature of 37°C), and the initial temperature was specified as the ambient value 25°C. The pressure outlet boundary condition was used at the top.

3.1 Turbulence model modification

A transient natural convection problem with fluid initially at rest can be characterised as an initially laminar flow with transition to turbulence. The selection of an appropriate turbulence model was therefore critical for the success of the numerical simulations, especially owing to the need for incorporating suitable physics of interfacial layer formation. Two alternative methods can be employed to render the Navier–Stokes equations tractable so that small-scale turbulent fluctuations do not have to be directly simulated; these are Reynolds-averaged (or ensemble-averaging) Navier–Stokes (RANS) or filtered Navier–Stokes equations (large eddy simulation (LES)). Both methods are available to exploit in Fluent, but LES requires significantly more computer resources in comparison with RANS models. After carefully considering available options and prospective application to real caverns, a decision was made to use the RANS shear-stress transport (SST) k–ω model. The SST k–ω model (Menter, 1994) is based on both the standard k–ω (Wilcox, 1998) and standard k–ε (Launder and Spalding, 1972) models, giving the accuracy of a k–ω model in the near-wall region and free-stream independence of the k–ε model in the far field. To achieve this, the k–ε model has been converted into a k–ω formulation including modifications for low-Reynolds-number effects, compressibility and shear flow spreading. A turbulent viscosity has been modified to account for turbulent shear-stress transport.

Note that turbulence is generated by the buoyancy term as well as local shear, the former playing a dominant role. A careful review of the equations for turbulent kinetic energy and dissipation rate (*Fluent 6.2 User's Guide* (Ansys, 2005)) indicated that buoyancy effects were not fully included in the original SST model. Therefore, the buoyancy influence was added to the production terms of the governing equations for turbulent kinetic energy and specific dissipation rate as a user-defined source term (G_b), namely

$$1. \quad G_b = -\boldsymbol{g}\frac{\mu_t}{\rho Pr_t}\frac{\partial \rho}{\partial z}$$

where the fluid density ρ is a function of temperature, salinity and pressure; $\boldsymbol{g}$ is the gravitational constant, μ_t is the turbulent viscosity; z is the vertical coordinate and Pr_t is the turbulent Prandtl number. The full description of different terms in the governing equations can be found in Appendix 1.

3.2 Geometry and grid generation

The simulations require high grid resolution surrounding the heated walls and density interfaces in order to resolve details of the boundary layer behaviour. The special grid generator of Fluent, Gambit version 2.4 (*Gambit 2.4 Tutorial Guide* (Ansys, 2007)), was used to create the required mesh. A cylinder with aspect ratio (H/d) equal to 8 was used, identical to the laboratory tank experiment (Figure 4). To reproduce the experimental conditions, two volumes were employed with different initial conditions for salinity. Two-dimensional axisymmetric models were used to reduce the computational time. A hexahedral stretched grid that provides better resolution of viscous gradients near the heated walls was used (Figure 5). A grid resolution study was performed using four stages of grid refinement. In these, the

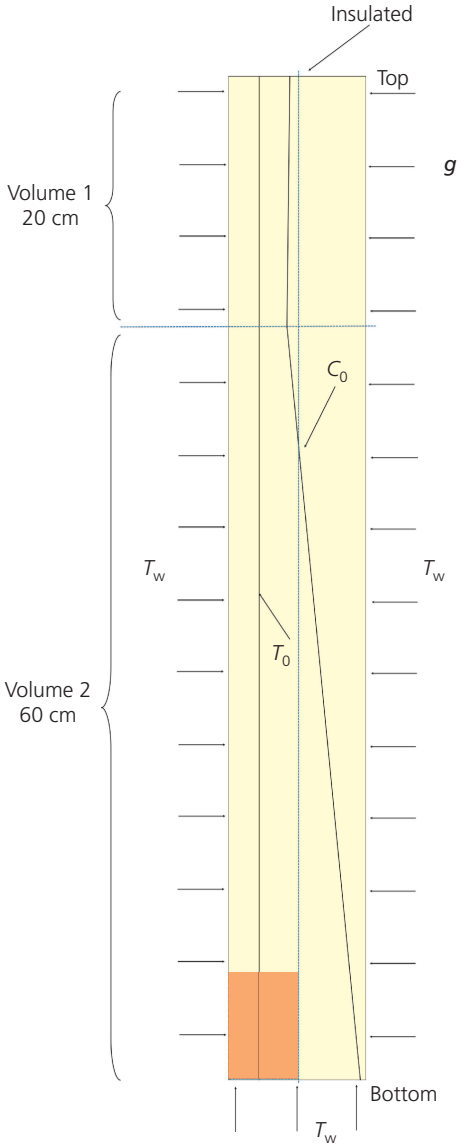

Figure 4. Model set-up (the shaded rectangle corresponds to the grid shown in Figure 5)

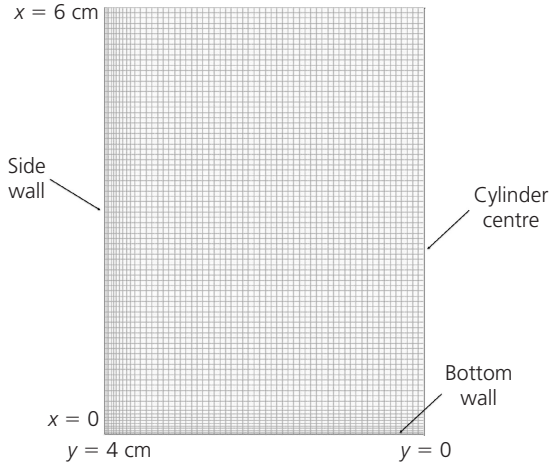

Figure 5. Part of the computational grid used for numerical simulations (see Figure 4)

same boundary layer resolution was used while decreasing the fixed grid step size beyond.

3.3 Initial and boundary conditions

To initialise the flow field, linear salinity profiles were used (Figure 6) with an initial temperature of 25°C. All input data were based on experimental measurements for the case shown; $N = 0{\cdot}44$/s and the initial temperature of the heated surfaces as 37°C, or an initial temperature difference between the heated surfaces and the interior fluid of 12°C.

A suitable equation of state for the working fluid (brine) was specified. In general, brine composition can vary from almost pure water to saturated saline solutions. Rowe and Chou (1970) presented a polynomial to calculate specific volume and compressibility of various salt solutions over a limited temperature range. Based on this work, and using additional data provided by Zarembo and Fedorov (1975) and Potter and Brown (1977), Batzle and Wang (1992) developed a simple polynomial that relates the density of brine to temperature, pressure and salinity. This polynomial (Equation 2) was used to calculate the density at each time step.

$$\begin{aligned}\rho_w &= 1 + 1e^{-6}(-80T - 3{\cdot}3T^2 + 0{\cdot}00175T^3 + 489p \\ &\quad - 2Tp + 0{\cdot}16T^2p - 1{\cdot}3e^{-5}T^3p - 0{\cdot}333p^2 \\ &\quad - 0{\cdot}02Tp^2) \\ \rho_b &= \rho_w + Y\{0{\cdot}668 + 0{\cdot}44Y + 1e^{-6}[300p - 240pY \\ &\quad + T(80 + 3T - 3300Y - 13p + 47pY)]\}\end{aligned} \quad (2)$$

where ρ_w and ρ_b are the densities of water and brine in g/cm^3, the pressure p is given in MPa, the temperature T in °C, and Y is the weight fraction (ppm/1000 000) of sodium chloride.

An additional polynomial was implemented into Fluent to specify thermal conductivity, based on Yusufova *et al.* (1975), see Equation 3 below. The latter authors used a combination of analysis and empirical correlations developed to describe thermal conductivity of aqueous sodium chloride as a function of concentration and temperature in the range 20–330°C and concentrations of 5, 10, 15, 20 and 25%. Ozbek and Phillips (1980) recommended the same empirical equations in their work after survey of the current experimental values reported in the literature for aqueous sodium chloride solutions.

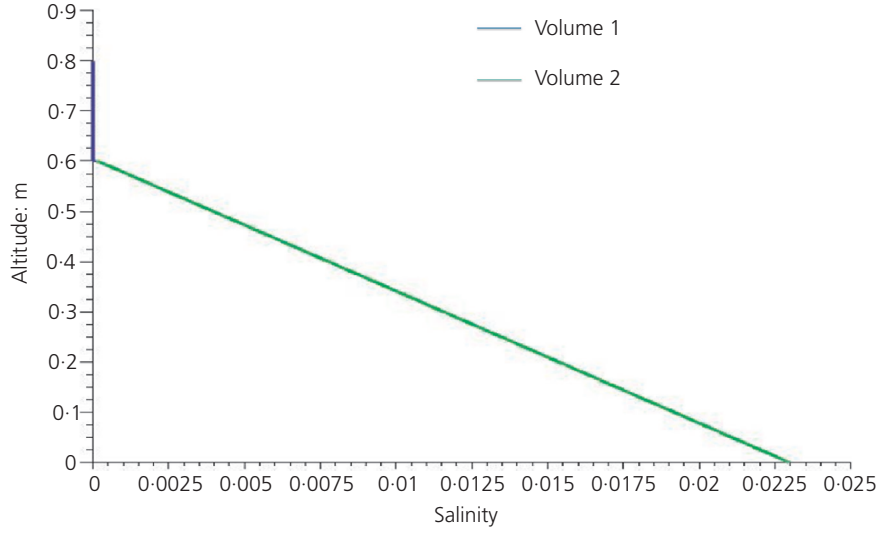

Figure 6. Initial profiles for (a) the salinity (initial gradient 0·038 m^{-1}) and (b) hydrostatic pressure

$$\begin{aligned}\lambda/\lambda_w = {} & 1{\cdot}0 - [2{\cdot}3434 \times 10^{-3} - (7{\cdot}924 \times 10^{-6})T \\ & + (3{\cdot}924 \times 10^{-8})T^2]S \\ & + [1{\cdot}06 \times 10^{-5} - (2 \times 10^{-8})T \\ & + (1{\cdot}2 \times 10^{-10})T^2]S^2 \\ \lambda_w = {} & - 0{\cdot}92247 + 2{\cdot}8395[(T + 273{\cdot}15)/273{\cdot}15] \\ & - 1{\cdot}8007[(T + 273{\cdot}15)/273{\cdot}15]^2 \\ & + 0{\cdot}52577[(T + 273{\cdot}15)/273{\cdot}15]^3 \\ & - 0{\cdot}07344[(T + 273{\cdot}15)/273{\cdot}15]^4 \end{aligned} \quad (3)$$

where the concentration of sodium chloride is given by

$$S = \frac{5844{\cdot}3 \text{ mol}}{1000 + 58{\cdot}443 \text{ mol}}$$

and λ_w is the thermal conductivity for pure water. The unit for temperature T is °C and the thermal conductivity is in W/m°K, which varies in the range 0·6–0·63 W/m°K in the present numerical simulations.

A relatively simple empirical fit was used for the dynamic viscosity of brine, as suggested by Hebert *et al.* (1988)

$$\mu = 1{\cdot}002 \times 10^{-3}(1 + 0{\cdot}4819Y - 0{\cdot}2774Y^2 + 0{\cdot}7814Y^3)$$

where Y is in ppb/1000.

Based on the above formulae, user-defined functions were developed and implemented to specify the density, thermal conductivity and viscosity of brine.

4. Results and discussion

Starting from the initial conditions, the momentum, energy and species equations were solved in time. In each time step, a number of iterations were needed to satisfy the convergence criterion. Initially, the liquid solution was motionless, stably stratified (species concentration decreases with height linearly) and isothermal (constant temperature in the entire volume). At time $t = 0$, a uniform temperature higher than the initial fluid temperature was applied with $\Delta T_0 = 12$°C, and the simulations were initialised with turbulence of low intensity (an initial turbulent kinetic energy was set up to 10^{-7} m^2/s^2).

Comparisons were made between laminar and turbulent flow calculations. Turbulent flows are characterised by fluctuating velocity fields that mix transported quantities such as momentum, energy and species concentration, and cause the transported quantities to fluctuate as well. The set of governing equations contains unknown variables, and turbulence models are needed to determine these variables in terms of known quantities and to close the set of equations. The two-equation SST k–ω model is used to determine the turbulent kinetic energy and specific dissipation rate in this study. Also compared were the computations of two turbulent flow cases where the default and modified (with an additional turbulent production term given by Equation 1) SST models were used. Vertical profiles of temperature and salinity were available from the experiment at three different times (2, 5 and 8 min), which were compared with the numerical outcomes. The results of the investigation provide insights into the growth and nature of the flow as well as the temperature and the concentration fields.

4.1 Comparison between laminar and turbulent flows

The temperature and salinity profiles obtained in laminar and two turbulent simulations are compared to clarify the layering mechanism. The measurements were made using an MCSTI probe (1·6 cm in diameter) that traversed vertically through the test fluid at a velocity of 0·5 cm/s. There was a small amount of unavoidable mixing in the wake of the probe, which reduced the gradients of temperature and salinity in the wake region. Owing to the low traverse velocity of the probe, it is reasonable to assume that the width of this wake is approximately the diameter of the probe. Therefore, the salinity and temperature numerical profiles were horizontally averaged over an area with 1 cm radius, centred at the probe tip, when comparing experiments. These comparisons show unambiguously the contribution of turbulence to mixing and formation of internal interfaces in the fluid. The temperature and salinity profiles at different times for laminar and turbulent flows (using the original and modified SST model) are shown in Figure 7, overlain by the measurements.

The temperature difference between the walls and the interior leads to fluid motions near the wall that are initially laminar and then turbulent. Turbulence accelerates the transfer processes and leads to faster layer formation than in the laminar case. Computations with the modified SST turbulent model gave results that better fit the measurements than those of the original (default) model.

The main difference between the modelled and experimental results occurs in profiles taken at 5 min, in that the evolution proceeds faster in the experiment than in numerical simulations, especially for temperature. The vertical layer heights agree well with the experiment. However, the temperature predictions do not agree well with the data. The temperature is underpredicted, probably owing to underestimation of horizontal mixing/diffusion by the model, which predicts stronger horizontal gradients than that in the experiment. This stronger horizontal gradient leads to lower temperatures towards the centre of the tank, as is evident from Figure 7. The disagreement between the modelled and experimental results is greater at the top modelled layer. One possible reason is the top boundary condition in the experiment,

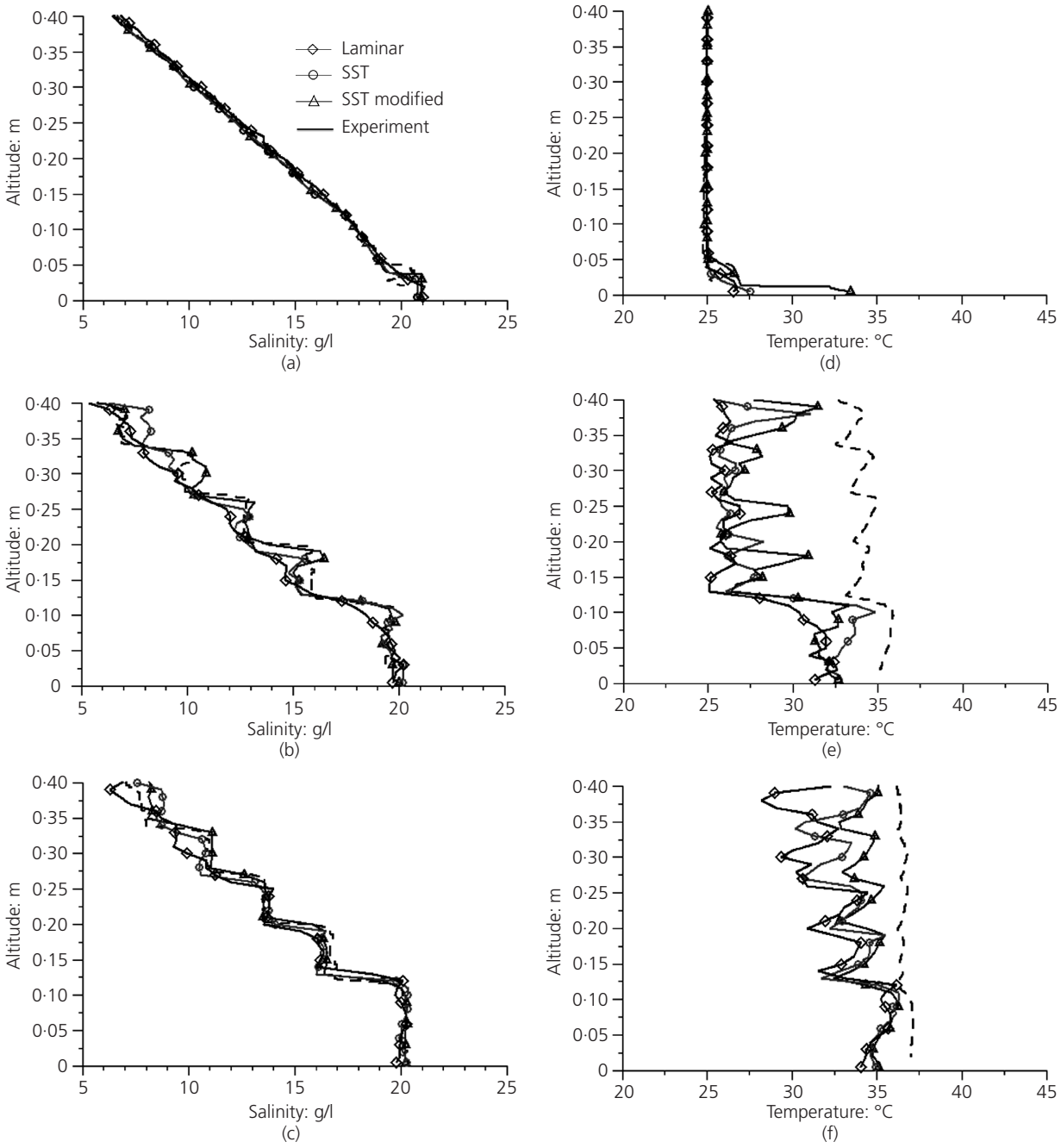

Figure 7. Comparison between the measured and simulated salinity (a)–(c) and temperature (d)–(f) profiles (averaged over 1 cm radius) for laminar and turbulent flows: original SST model and modified SST model; different times are shown: (a) 2 min; (b) 5 min; (c) 8 min; (d) 2 min; (e) 5 min; (f) 8 min after the beginning of heating

which was left open to the free atmosphere and hence was ill-defined.

The run time of the numerical calculations was not sufficient to obtain the eventual fully mixed flow with a steady temperature gradient. The simulations were continued up to 15 min, consistent with the laboratory experiment run time. Figure 8 shows the vertical salinity and temperature profiles obtained using the modified SST model 15 min after the beginning of heating and their comparison with the experimental data at 8 min. Note that the laboratory experiments appeared to be fully evolved into layers after 8 min whereas the same developments in the simula-

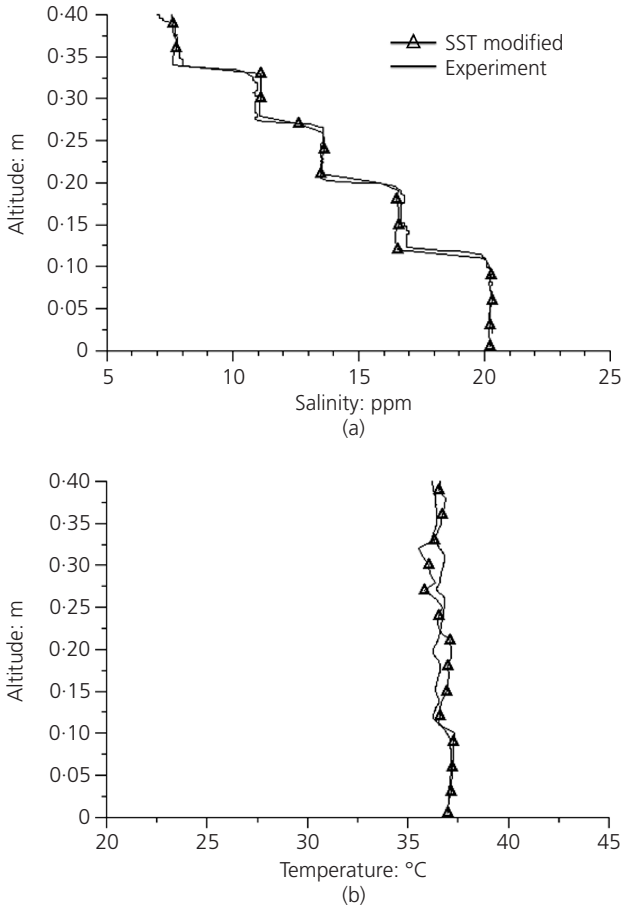

Figure 8. Comparison between simulated and experimental results for (a) salinity and (b) temperature vertical profiles obtained with modified SST turbulent model 15 min after the beginning of heating, with the experimental profiles registered at time 8 min

tions required about 15 min; thus, in comparisons, information obtained using these two times are used.

Table 1 gives further quantitative analysis of results in terms of statistical measures such as mean fractional errors (MFE) and bias (MFB), mean absolute error (MAE), root mean square error (RMSE) and index of agreement (IA). Their definitions are given in Appendix 2. The modified SST model provides predictions that are in best agreement with the experiment, and extending the time of numerical calculations up to 15 min improves the results for both profiles.

4.2 Grid independence study

Four different grids were employed with the modified SST model. The same boundary layer resolution was maintained while decreasing the fixed grid step outside the boundary layer. The height of the first boundary layer row was 0·01 cm, beyond which the grid step was first increased with a growth factor of 1·2 up to several selected rows (which vary on the grid system) while specifying a fixed grid step thereafter. The grid refinement was made using 0·1, 0·07, 0·05 and 0·03 cm grid steps for different meshes above the boundary layer. First, the so-called 'rough' mesh, which included 47 328 cells, was used to 'tune' the physical model parameters by seeking the best fit to experimental results. Three additional grids – 'coarse' (89 397 cells), 'fine' (167 648 cells) and 'finer' (457 596 cells) – were also employed. Comparison between salinity and temperature profiles for all grids is shown in Figure 9. The results did not change dramatically, and important features associated with this doubly diffusive flow were captured by all four grids. Simulations using the rough and coarse grids, however, could not predict the heights of layers in the experiment well. The differences between fine and finer grid results were insignificant, and both provided very good agreement with the measurements.

	Salinity				
	MFE: %	MFB: %	MAE: g/l	RMSE: g/l	IA
LAM	11·84	3·35	0·81	1·04	0·992
SST	14·78	4·85	0·71	1·01	0·992
SSTmod (8 min)	6·72	−0·58	0·47	0·74	0·996
SSTmod (15 min)	5·84	0·89	0·39	0·67	0·997
	Temperature				
	MFE: %	MFB: %	MAE: °C	RMSE: °C	IA
LAM	11·68	11·68	3·96	4·52	0·990
SST	8·97	8·97	3·06	3·74	0·993
SSTmod (8 min)	7·88	7·88	2·70	3·40	0·994
SSTmod (15 min)	2·70	1·77	0·91	2·16	0·998

Table 1. Quantitative analysis of salinity and temperature

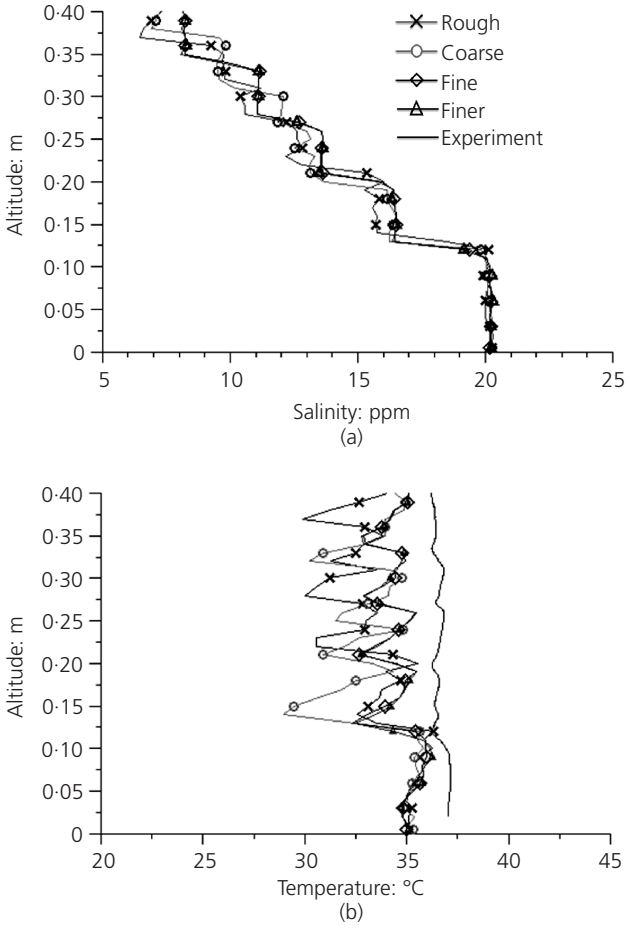

Figure 9. The effect of grid resolution on (a) salinity and (b) temperature profiles; measured and simulated (averaged over 1 cm radius) for rough, coarse, fine and finer grids; plots 8 min after the beginning of heating are shown

Table 2 provides statistical measures of model performance by comparing predictions and observations. The errors decrease with grid refinement, but there is no significant difference between the fine and finer grids. The fine grid is the best choice in terms of the quality of results and computational time. Note the excellent index of agreement (the perfect fit is when IA = 1).

4.3 Qualitative study of flow development

The time evolution of the flow is displayed by salinity and temperature plots in Figures 10 and 11 respectively. Results from the fine grid are presented. At early times, flow activities are prevalent near the heated walls, and these grow and penetrate the fluid interior. The bottom layer is the most active at the onset because of combined forcing from the bottom and lateral walls. When instability sets in, salty fluid parcels are lifted by the buoyant wall layer up to their neutrally stratified level, and then 'collapse' to form intrusive structures propagating into the interior. Note that faster diffusion of heat causes these intrusions to cool (transferring heat to the interior fluid) and lose buoyancy, thus propagating slant-wise. The collapse of rising fluid and the formation of bottom mixing layer are soon followed by the formation of the rest of the layers by way of a similar mechanism, but the latter only involves side-wall thermal forcing. The simulations clearly show that the development of mixed layers is caused by the merging of slanted intrusions emanating from the side walls and their subsequent downward penetration. The rise of fluid near the walls and descent near the centre generate recirculating cells in each of the layers. In the bottom layer, however, the descending motions are countered by the ascending motions from the bottom wall, and a complicated flow pattern emerges at the middle of the layer, which is somewhat similar to a stagnation flow pattern around a rising plume (Figure 12). The plume is slowly eroded laterally while amplifying along the axis (see Ching *et al.*, 1995). The heat and salt fluxes across diffusive interfaces formed between the layers appear to play a lesser role

	MFE	MFB	MAE	RMSE	IA
			Salinity		
Rough	11·84	3·35	0·81	1·04	0·992
Coarse	14·78	4·85	0·71	1·01	0·992
Fine	6·72	−0·58	0·47	0·74	0·996
Finer	5·84	0·89	0·39	0·67	0·997
			Temperature		
Rough	11·68	11·68	3·96	4·52	0·990
Coarse	8·97	8·97	3·06	3·74	0·993
Fine	7·88	7·88	2·70	3·40	0·994
Finer	2·70	1·77	0·91	2·16	0·998

Table 2. Quantitative analysis of salinity and temperature for different grids

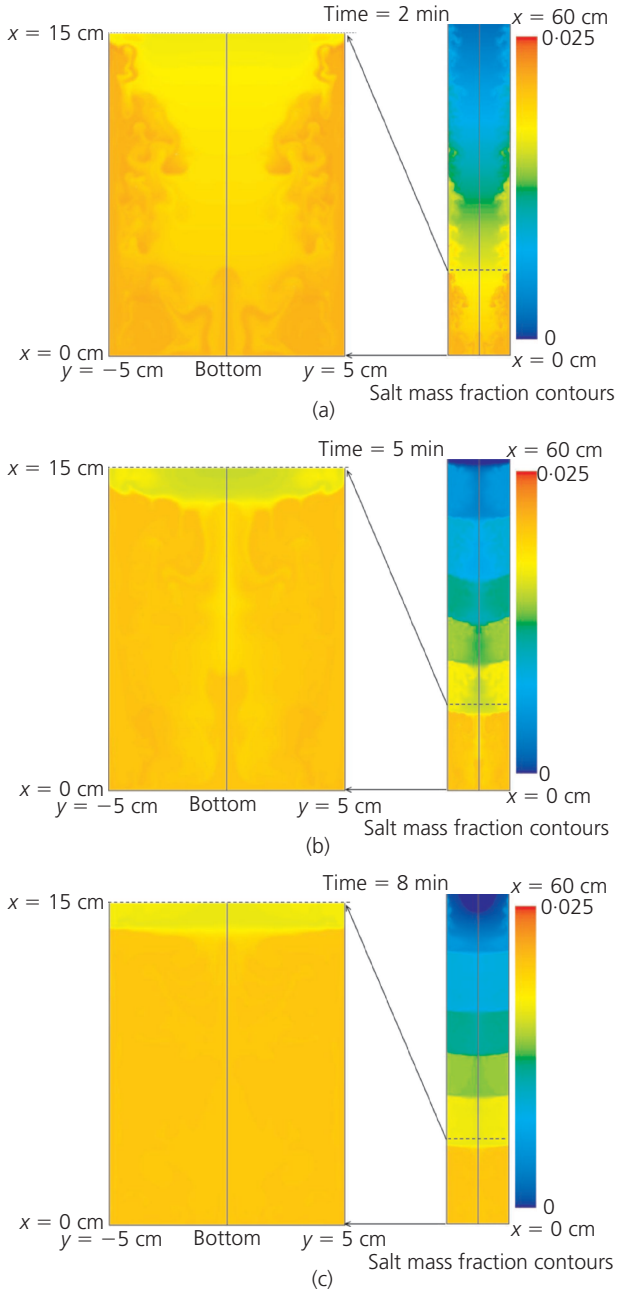

Figure 10. Simulated salinity at 2, 5 and 8 min after the beginning of heating

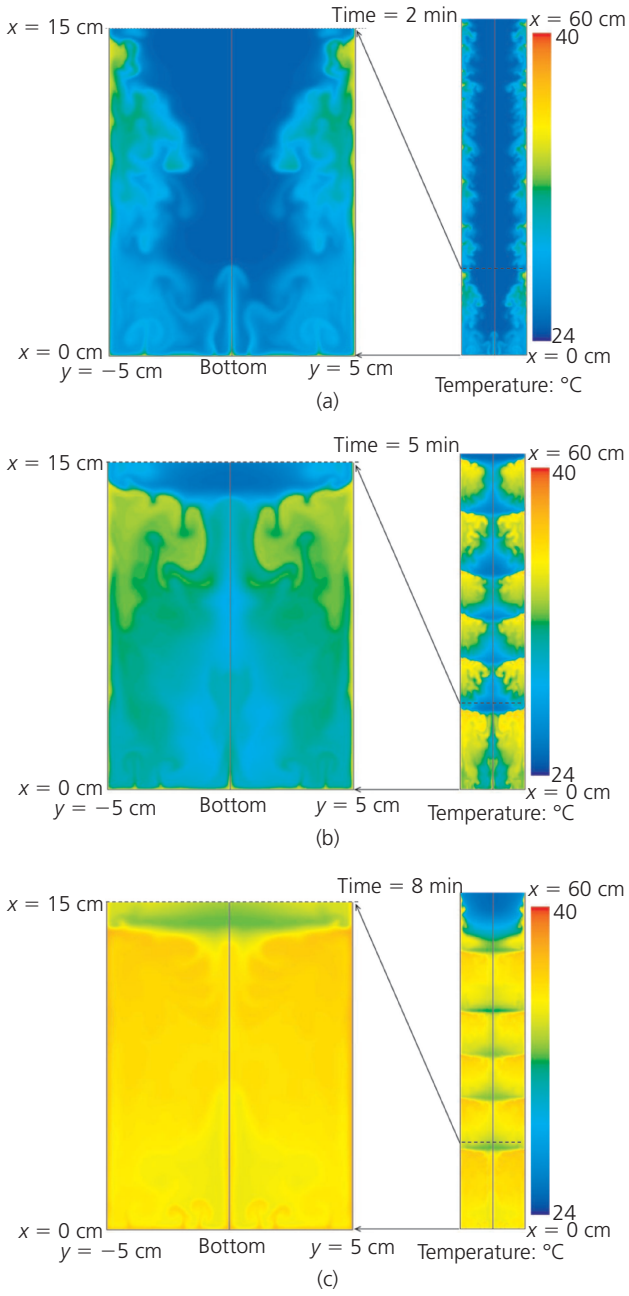

Figure 11. Simulated temperature 2, 5 and 8 min after the beginning of heating

in the initial evolution of the layers, except that they are strong enough to prevent turbulent eddies penetrating through them and destroying the layered structure.

4.4 Layer thicknesses

The layer thicknesses are approximately the same except for the bottom layer where thermal forcing occurs from the sides and the bottom. As evident from the previous section, the formation of the topmost layers is independent of the bottom layer and determined by the side-wall heating only, and thus the present work has similarities to the flow configuration used by Thorpe *et al.* (1969), albeit only one side wall of a rectangular box was heated in their experiment. The experiments of Thorpe *et al.* (1969) had well-defined side-wall boundary conditions – fixed wall temperature, no-slip conditions and no salt flux through the vertical walls – all of which are consistent with the present study's numerical calculations. Linear stability analysis of a narrow slot configuration showed the formation of thin horizontal layers of constant height δ that are dependent on the initial density gradient and thermal forcing (specified by the temperature

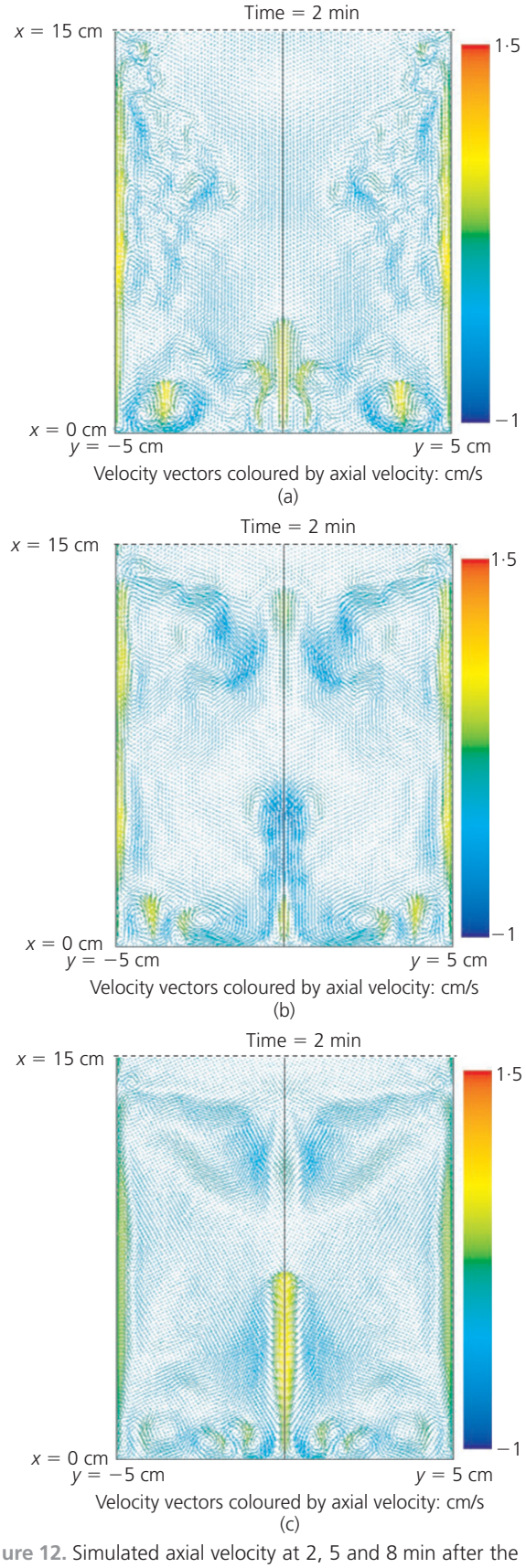

Figure 12. Simulated axial velocity at 2, 5 and 8 min after the beginning of heating

difference between the plates). The layer thickness was proportional to $\alpha\Delta T_0/(\beta\overline{S}_{z0})$ or $\delta \approx \Delta b/N^2$, where $N^2 = \boldsymbol{g}\beta\overline{S}_z$ is the initial buoyancy frequency, $\Delta b = \boldsymbol{g}\alpha\Delta T_0$ is the initial difference,

$$\beta = -\frac{1}{\rho_0}(\partial\rho/\partial S)_{P,T}$$

is the salinity contraction coefficient and

$$\alpha = -\frac{1}{\rho_0}(\partial\rho/\partial T)_{P,S}$$

is the thermal expansion coefficient.

Using numerical results, the thicknesses δ of several layers, excluding the bottom layer, were calculated and normalised by $\Delta b/N^2$. The numerical values in relation to the laboratory experimental values are shown in Table 3.

Different layer heights reckoned from the experiment and numerical modelling, including the bottom layer, are shown in Figure 13 alongside a salinity profile taken at a time of 8 min after the beginning of heating (Figure 13). The agreement between the numerical simulations and experimental data is excellent.

Note that the layer thickness $\delta \sim \Delta b/N^2$ in the fully turbulent state indicates the role of buoyancy and inertial forces of eddies in determining the sizes of the layers. On dimensional grounds, the convective velocity of the eddies can be written as $w_c = (\Delta b\delta)^{1/2}$, yielding a characteristic vertical inertia force of the order w_c^2/δ, which is to be balanced by the buoyancy forces $N^2\delta$ in determining the vertical thickness. This balance gives the observed vertical layer thickness. In addition, it is possible to show that under these buoyancy-inertia dominated conditions, δ also has a relationship with the Ozmidov length scale $\delta \sim (\varepsilon/N^3)^{1/2}$ (Fernando, 1987, 1988), and the data from the present study show that $\delta \approx 10(\varepsilon/N^3)^{1/2}$, which is in agreement with the previous findings from laboratory experiments (De Silva and Fernando, 1992).

Normalised thickness	Modelling	Experiment
$\delta_1 N^2/\Delta b$	1·15	1·17
$\delta_2 N^2/\Delta b$	1·15	1·16
$\delta_3 N^2/\Delta b$	1·00	1·00
Averaged	1·17	1·10
Standard deviation	±0·14	±0·07

Table 3. $\delta N^2/\Delta b$ (Thorpe *et al.*, 1969) obtained from modelling and experiment

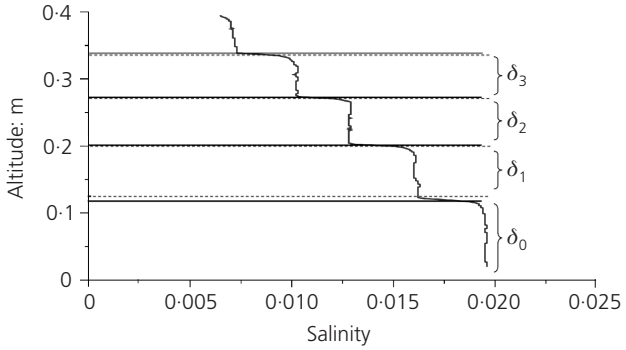

Figure 13. Sketch of different layers evaluated from the experiment (dashed line) and numerical modelling (solid line), superimposed on the vertical experimental salinity profile obtained at time $t = 8$ min

5. Conclusions

The efficacy of a shear-stress transport (SST) k–ω model within the Fluent commercial software to simulate the heating of a stable salinity gradient in a low-aspect-ratio container was investigated. The heat was supplied from the bottom and sides, in the form of elevated wall temperatures, and the SST k–ω model in Fluent was modified to account explicitly for strong buoyancy effects. A laboratory experiment was also conducted in parallel to help evaluate the model, for which statistical measures were employed. The aim was to validate the model so that it could be applied to the US SPRs.

Upon the supply of heat, a series of convective layers was formed following the breakdown of the salinity gradient first near the bottom and then along the walls. Mechanisms of their formation were delineated. The layers were of approximately equal height, except the bottom layer, which was thicker owing to enhanced thermal forcing from the sides and the bottom. The simulation and experimental results matched exceedingly well for the cases of bottom and upper layer heights. Good agreement was also noted with the theoretical and experimental work of Thorpe *et al.* (1969), who considered a somewhat different flow configuration that exhibits similar physical mechanisms. Under fully developed turbulent flow conditions, the layer height observed indicated that there is a balance between vertical inertia forces of convective eddies and buoyancy forces. With regard to temperature profiles, however, the agreement was not so good, mainly because of inadequate horizontal diffusion in numerical simulations compared to experiments. In the simulations, a constant temperature profile was achieved 15 min after the beginning of the simulations, whereas in the experiments this occurred within 8 min. Indications are that the model performance can be improved by better turbulence closure, perhaps by inclusion of additional terms to improve horizontal property transports. Another issue is the initialisation of turbulence. In the laboratory, the flow is initially laminar and then transitions to turbulence flow, which is not replicated by the turbulent flow simulations conducted here. Therefore, an initial turbulence level had to be specified, which was rather arbitrary.

The faster horizontal response in the experiments is also aided by the collapse of convective mixed layers formed at the side walls, which is not directly captured and parameterised by the modelling procedure used. To account for this collapse it is necessary to include a turbulence model that appropriately considers the inhibition of the growth of turbulence scales by stable stratification (e.g. Noh and Fernando, 1991). Any future modifications to the turbulence model should include such intricate features.

Acknowledgements

The present work was carried out within the project 'Compositional convection in subterranean oil storage tanks' supported by Sandia National Laboratories. Sandia National Laboratories is a multi-programme laboratory operated by Sandia Corporation, a wholly owned subsidiary of Lockheed Martin Company, for the US Department of Energy's National Nuclear Security Administration under contract DE-AC04–94AL85000. Special thanks are given to Professor Darryl James from Texas Tech University who helped with the development of the user-defined function for the brine density.

Appendix 1

Shear-stress transport (SST) k–ω model – modification

The buoyancy effects were added to the production terms of the governing equations (*Fluent 6.2 User's Guide* (Ansys, 2005)) as an additional source term G_b

$$\frac{\partial}{\partial t}(\rho k) + \frac{\partial}{\partial x_i}(\rho k u_i) = \frac{\partial}{\partial x_j}\left(\Gamma_k \frac{\partial k}{\partial x_j}\right) + \tilde{G}_k - \Lambda_k + G_b$$

$$\frac{\partial}{\partial t}(\rho \omega) + \frac{\partial}{\partial x_i}(\rho \omega u_i) = \frac{\partial}{\partial x_j}\left(\Gamma_\omega \frac{\partial \omega}{\partial x_j}\right) + G'_\omega - \Lambda_\omega + D_\omega$$

where G_k represents the generation of turbulent kinetic energy due to mean velocity gradients; G_b represents the generation due to buoyancy effects; G'_ω represents the generation of ω, including the effects of buoyancy; Γ_k and Γ_ω represent the effective diffusivity of k and ω, respectively; Λ_k and Λ_ω represent the dissipation of k and ω due to turbulence; D_ω represents the cross-diffusion term. The indices i, j here indicate different axes. The buoyancy was added as user-defined source terms in both equations for the two-dimensional case.

New turbulent production terms $\tilde{G}'_k$, G'_ω

The new production term in the equation of turbulent kinetic energy can be described by new variable $\tilde{G}'_k = \min(G'_k,\ 10\rho\beta^*_i k\omega)$, where $G'_k = G_k + G_b$ represents the production of turbulent kinetic energy, including buoyancy effects, by a function

$$G_b = -\boldsymbol{g}_i \frac{\mu_t}{\rho Pr_t}\frac{\partial \rho}{\partial x_i}$$

where μ_t is turbulent viscosity, $\boldsymbol{g}_i$ is the components of gravitational vector, ρ is fluid density; $Pr_t = 1/\alpha$ is a turbulent Prandtl number.

$$G_k = \rho\overline{u'_i u'_j}\frac{\partial u_j}{\partial x_i} = \mu_t S^2,\ \ S$$

where S is the modulus of the mean rate-of-strain tensor $S = \sqrt{2S_{ij}S_{ij}}$ with components

$$S_{ij} = \frac{1}{2}\frac{\partial u_j}{\partial x_i} + \frac{\partial u_i}{\partial x_j}$$

The turbulent viscosity can be represented by the relation

$$\mu_t = \frac{\rho k}{\omega}\frac{1}{\max\left[\frac{1}{\alpha^*}, \frac{SF_2}{a_1\omega}\right]}$$

with the coefficient that damps the turbulent viscosity (by way of a low-Reynolds-number correction) given by

$$\alpha^* = \alpha^*_\infty\left(\frac{\alpha^*_0 + Re_t/R_k}{1 + Re_t/R_k}\right)$$

where Reynolds turbulent number is

$$Re_t = \frac{\rho k}{\mu\omega}$$

and all other parameters are constants ($R_k = 6$; $\alpha^*_0 = \beta_i/3$; $\beta_i = 0{\cdot}072$).

The production of ω is given by

$$G_\omega = \frac{\rho\alpha}{\mu_t}G'_k$$

with coefficient

$$\alpha = \frac{\alpha_\infty}{\alpha^*}\left(\frac{\alpha_0 + Re_t/R_\omega}{1 + Re_t/R_\omega}\right)$$

where

$$R_\omega = 2{\cdot}95\,\alpha^*$$

$$\alpha_0 = \frac{1}{9}$$

$$\alpha_\infty = F_1\alpha_{\infty,1} + (1 - F_1)\alpha_{\infty,2}$$

$$\alpha_{\infty,1} = \frac{\beta_{i,1}}{\beta^*_\infty}\frac{\kappa^2}{\sigma_{\omega,1}\sqrt{\beta^*_\infty}}$$

$$\alpha_{\infty,2} = \frac{\beta_{i,2}}{\beta^*_\infty}\frac{\kappa^2}{\sigma_{\omega,2}\sqrt{\beta^*_\infty}}$$

κ is 0·41, $\beta_{i,1} = 0{\cdot}075$, $\beta_{i,2} = 0{\cdot}0828$, $\sigma_{\omega,1} = 2{\cdot}0$, $\sigma_{\omega,2} = 1{\cdot}168$. Note that, in high-Reynolds-number form of the k–ω model, $\alpha = \alpha_\infty = 1$.

Turbulent dissipation Λ_k, Λ_ω

The dissipation of turbulent kinetic energy can be defined by: $\Lambda_k = \rho\beta^*_i k\omega$ with

$$\beta^*_i = \beta^*_\infty\frac{4/15 + (Re_t/R_\beta)^4}{1 + (Re_t/R_\beta)^4}$$

The dissipation of ω can be defined by: $\Lambda_\omega = \rho\beta_i\omega^2$ with $\beta_i = F_1\beta_{i,1} + (1 - F_2)\beta_{i,2}$, where F_1, F_2 are blending functions $F_1 = f(k, \omega, \mu, \rho, y, D_\omega{}^+)$, $F_2 = f(k, \omega, \mu, \rho, y)$.

Effective diffusivity

The effective diffusivities for the SST k–ω model are given by

$$\Gamma_k = \mu + \frac{\mu_t}{\sigma_k}$$

$$\Gamma_\omega = \mu + \frac{\mu_t}{\sigma_\omega}$$

where σ_k and σ_ω are the turbulent Prandtl number for k and ω respectively

$$\sigma_k = \frac{1}{F_1/\sigma_{k,1} + (1 - F_2)/\sigma_{k,2}}$$

$$\sigma_\omega = \frac{1}{F_1/\sigma_{\omega,1} + (1 - F_2)/\sigma_{\omega,2}}$$

Cross-diffusion modification

The SST k–ω model is based on both the standard k–ω model and the standard k–ε model. To blend these two models together, the standard k–ε model has been transformed into equations based on k and ω, which leads to the introduction of a cross-diffusion term D_ω defined as

$$D_\omega = 2(1 - F_1)\rho\sigma_{\omega,2}\frac{1}{\omega}\frac{\partial k}{\partial x_j}\frac{\partial \omega}{\partial x_j}$$

Appendix 2

The following indicators were used for performance evaluation. Here the letters denote: M modelled; E experimental; $\overline{E}$ averaged experimental outcomes; N samples number

Mean fractional bias

$$\mathrm{MFB} = \frac{2}{N}\sum_{i=1}^{N}\frac{(M_i - E_i)}{(M_i + E_i)}$$

Mean fractional error

$$\mathrm{MFE} = \frac{2}{N}\sum_{i=1}^{N}\frac{|M_i - E_i|}{|M_i + E_i|}$$

Root mean square error

$$\mathrm{RMSE} = \sqrt{\frac{\sum_{i=1}^{N}(M_i - E_i)^2}{N}}$$

Index of agreement

$$\mathrm{IA} = 1 - \frac{\sum_{i=1}^{N}(M_i - E_i)^2}{\sum_{i=1}^{N}\left(|M_i - \overline{E}| + |E_i - \overline{E}|\right)^2}$$

REFERENCES

Ansys (2005) *Fluent 6.2 User's Guide*. Ansys, Canonsburg, PA, USA. See http://www.ansys.com/Products/Simulation+Technology/Fluid+Dynamics/ANSYS+Fluent (accessed 15/11/2011).

Ansys (2007) *Gambit 2.4 Tutorial Guide*. Ansys, Canonsburg, PA, USA. See http://my.fit.edu/itresources/manuals/gambit/pdf/tg/tgtoc.pdf (accessed 15/11/2011).

Batzle M and Wang Zh (1992) Seismic properties of pore fluids. *Geophysics* **97(11)**: 1396–1408.

Brandt A and Fernando HJS (eds) (1996) Double-diffusive convection. In *American Geophysical Union Monograph*. American Geophysical Union, Washington DC, vol. 94.

Chen CF, Briggs DG and Wirtz RA (1971) Stability of thermal convection in a salinity gradient due to lateral heating. *International Journal of Heat and Mass Transfer* **14(1)**: 51–65.

Ching CY, Fernando HJS and Robles A (1995) Breakdown of line plumes in turbulent environments. *Journal of Geophysical Research (Oceans)* **100(C3)**: 4707–4713.

De Silva IPD and Fernando HJS (1992) Some aspects of mixing in stratified turbulent path. *Journal of Fluid Mechanics* **240**: 601–625.

Fedorovich E and Shapiro A (2009) Turbulent natural convection along a vertical plate immersed in a stably stratified fluid. *Journal of Fluid Mechanics* **636**: 41–57.

Fernando HJS (1987) Formation of a layered structure when a stable salinity gradient is heated from below. *Journal of Fluid Mechanics* **182**: 525–541.

Fernando HJS (1988) The growth of a turbulent patch in a stratified fluid. *Journal of Fluid Mechanics* **190**: 55–70.

Fernando HJS (1989) Buoyancy transfer across a diffusive interface. *Journal of Fluid Mechanics* **209**: 1–34.

Hebert A, Jacson C and Lever D (1988) Coupled groundwater flow and solute transport with fluid density strong dependent upon concentration. *Water Resources Research* **24(10)**: 1781–1795.

Huppert HE and Turner JS (1981) Double-diffusive convection. *Journal of Fluid Mechanics* **106**: 299–329.

Huppert HE, Kerr RC and Hallworth MA (1984) Heating or cooling a stable compositional gradient from the side. *International Journal of Heat and Mass Transfer* **27(8)**: 1395–1401.

Hyun JM and Lee JW (1989) Numerical solutions for transient natural convection in a square cavity with different sidewall

temperatures. *International Journal of Heat and Fluid Flow* **10(2)**: 146–151.

Kelly D, Fernando HJS, Gargett A, Tanny J and Ozoy E (2003) The diffusive regime of double-diffusive convection: laboratory and observational aspects. *Progress in Oceanography* **56(3–4)**: 461–481.

Launder BE and Spalding DB (1972) *Lectures in Mathematical Models of Turbulence*. Academic Press, London, UK.

Lee JW and Hyun JM (1991) Double diffusive convection in a cavity under a vertical solutal gradient and a horizontal temperature gradient. *International Journal of Heat and Mass Transfer* **34(9)**: 2423–2427.

Lee J, Hyun MT and Kim KW (1988) Natural convection in confined fluids with combined horizontal temperature and concentration gradients. *Journal of Heat and Mass Transfer* **31(10)**: 1969–1977.

Lin W and Armfield SW (1999) Direct simulation of natural convection cooling in vertical circular cylinder. *International Journal of Heat and Mass Transfer* **42(22)**: 4117–4130.

Menter FR (1994) Two-equation eddy-viscosity turbulence models for engineering applications. *AIAA Journal* **32(8)**: 1598–1605.

Nishimura T, Ogata Y, Sakura S and Morega AM (1999) Interfacial breakdown of double diffusive convective layers by a horizontal temperature gradient. *International Journal of Heat and Mass Transfer* **42(8)**: 1479–1489.

Noh Y and Fernando HJS (1991) A numerical study on the formation of a thermocline in shear-free turbulence. *Physics of Fluids* **A3(3)**: 422–426.

Oster G and Yamamoto M (1963) Density gradient techniques. *Chemical Reviews* **63(3)**: 257–268.

Ozbek H and Phillips SL (1980) Thermal conductivity of aqueous sodium chloride solution from 20 to 330°C. *Journal of Chemical and Engineering Data* **25(3)**: 263–267.

Pol SU (2010) *Evolution of Convection and Turbulent Jets in Stratified Low Aspect Ratio Containers*. PhD thesis, Arizona State University, Arizona, USA.

Potter RW and Brown DL (1977) The volumetric properties of sodium chloride solutions from 0° to 500°C at pressures up to 2000 bars based on a regression of available data in the literature. *US Geological Survey Bulletin* **1421-C**, doi 10.2172/7310721 (available at: http://www.osti.gov/bridge/product.biblio-jsp?ostiid=7310721, accessed 14/11/2011).

Rowe AM and Chou JCS (1970) Pressure–volume–temperature–concentration relation of aqueous NaCl solutions. *Journal of Chemical and Engineering Data* **15(1)**: 61–66.

Suzukawa Y and Narusawa U (1982) Structure of growing double-diffusive convection cells. *Journal of Heat Transfer* **104(2)**: 248–254.

Thorpe SA, Hutt PK and Soulsby R (1969) The effect of horizontal gradients on thermohaline convection. *Journal of Fluid Mechanics* **38(pm-t 2)**: 375–400.

Turner JS (1967) Salt fingers across a density interface. *Deep-Sea Research* **14**: 599–611.

Turner JS (1974) Double diffusive phenomena. *Annual Review of Fluid Mechanics* **6**: 37–56.

Turner JS (1985) Multicomponent convection. *Annual Review of Fluid Mechanics* **17**: 11–44.

Wilcox DC (1998) *Turbulence Modeling for CFD.* DCW Industries Inc., La Canada, California, USA.

Yusufova VD, Pepinov RI, Nikolaev VA and Guseinov GM (1975) Thermal conductivity of aqueous solutions of NaCl. *Inzhenerno-Fizicheskii Zhurnal* **29**: 600.

Zarembo VI and Fedorov MK (1975) Density of sodium chloride solutions in the temperature range 25–350°C at pressures up to 1000 kg/cm^3. *Journal of Applied Chemistry USSR* **48**: 1949–1953 (English translation).